Photoanodic H₂O₂ synthesis and *in-situ* tetracycline degradation using transition-metal phosphide co-catalysts

Yuntao Xu [a], Yongxin Pan [a], Wu Yahan [a], Yuanxing Fang [a,*], Masakazu Anpo [a], Hisao Yoshida [c,d], Xinchen Wang [a,b,**]

[a] State Key Laboratory of Photocatalysis on Energy and Environment, College of Chemistry, Fuzhou University, Fuzhou 350116, PR China
[b] Fujian Science & Technology Innovation Laboratory for Chemical Engineering of China, Quanzhou 362114, PR China
[c] Elements Strategy Initiative for Catalysts & Batteries (ESICB), Kyoto University, Kyoto 615-8245, Japan
[d] Department of Interdisciplinary Environment, Graduate School of Human and Environmental Studies, Kyoto University, Kyoto 615-8245, Japan
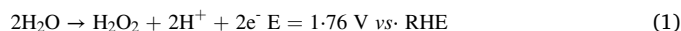
ARTICLE INFO

ABSTRACT

H_2O_2 as an essential chemical can be produced by photoanodic water oxidation reaction but is restricted by low production rate and poor selectivity. Herein, three kinds of transition metal phosphide, namely Fe_2P, Co_2P, and Ni_5P_4, have been loaded on Mo doped $BiVO_4$ (MB) photoanodes to promote H_2O_2 production. Among them, the optimal performance has been achieved by Ni_5P_4/MB photoanode with the yield of 20.8 μmol h⁻¹ cm⁻² and the selectivity of 41.9 % at the applied voltage of 1.7 V (vs. RHE) under AM 1.5 G illumination. By loading Ni_5P_4 on MB, the production rate of OH• radicals and the desorption of the as-formed H_2O_2 have been promoted. The intermediates, OH• radicals, have been in-situ applied for tetracycline degradation, and Ni_5P_4/MB photoanode presents the best performance. This work has demonstrated the developments of metal phosphide as co-catalysts for photoanodic H_2O_2 production from water and meanwhile paved the pathway for its in-situ use in water disinfectant.

1. Introduction

H_2O_2 is an essential chemical that is widely used for disinfectants, industry, surgery, and many others owing to its property as a strong oxidizing or reducing agent [1–3]. As a typical example, modern water treatment typically uses chlorination, but the concern is around the chemical residues for secondary pollution. Alternatively, the use of H_2O_2 to drive advanced oxidative processes is promising for water purification [4–6]. During the process, H_2O_2 would combine with a certain metal compound and light illumination to form hydroxyl (OH•) radicals. The OH• radicals would oxidize the organic compounds for degradation, resulting in green residues, namely O_2 and H_2O [7]. However, H_2O_2 is currently produced by the anthraquinone method, which is a hazardous approach with a high cost, restricting its practical application [8].

Photoanodic H_2O_2 synthesis is a green and sustainable approach since this reaction uses water as the sole reactant and is mainly driven by sunlight. The obstacle of this reaction is selective production because the H_2O_2 production reaction is competing with the oxygen evolution

reaction. In thermodynamics, the production of H_2O_2 has a required energy of 354 kJ mol⁻¹, which is higher than that for O_2 evolution (237 kJ mol⁻¹). Correspondingly, the lowest equilibrium potentials are 1.76 V versus reversible hydrogen electrode (vs. RHE) for oxidizing H_2O to H_2O_2 (Eqs. 1) and 1.23 V (vs. RHE) for oxidizing H_2O to O_2 (Eq. 2). Therefore, most of the photoanodes favor driving oxygen evolution reaction from water, such as $BiVO_4$ [9], TiO_2 [10,11], WO_3 [12], Fe_2O_3 [13] and many others [14–16].

$$2H_2O \rightarrow H_2O_2 + 2H^+ + 2e^-\ E = 1\cdot76\ V\ vs\cdot RHE \qquad (1)$$

$$2H_2O \rightarrow O_2 + 4H^+ + 4e^-\ E = 1\cdot23\ V\ vs\cdot RHE \qquad (2)$$

Co-catalyst is considered the key to improving both the yield and selectivity for H_2O_2 production, and a variety of materials have been developed to load on the surface of a photoanode, such as SnO_x [17], Al_2O_3 [18], Co_3O_4 [19], and others [20]. Among them, cobalt phosphide has been studied recently. In this structure, the Co site promotes the formation of OH• radicals by dissociating water molecules, and the P site

---

plays the role for H_2O_2 desorption from the surface [21]. Compared with cobalt phosphide, other transition-metal phosphide (TMP) materials are also potential to promote photoanodic H_2O_2 production, such as Fe_2P [22], Ni_5P_4 [23], and others [24,25], since they had presented excellent performances in the electrochemical system for the water oxidation reaction.

Herein, TMP materials, including Fe_2P, Co_2P, and Ni_5P_4, were synthesized and applied as co-catalysts on Mo doped $BiVO_4$ (MB) photoanode to promote H_2O_2 production. An optimal performance has been realized by Ni_5P_4/MB photoanode, and specifically, the yield and selectivity for H_2O_2 production are 20.8 $\mu mol \cdot h^{-1} \cdot cm^{-2}$ and 41.9 %, respectively, at a voltage bias of 1.7 V *vs.* RHE under sunlight illumination (AM 1.5 G). This production rate is ca. 5 times of the pristine $BiVO_4$ (BVO) photoanode. The improved performance of Ni_5P_4/MB photoanode for H_2O_2 production has been investigated. $OH^\bullet$ radicals are considered as the key intermediate for H_2O_2 synthesis, and by loading Ni_5P_4 co-catalyst, the production rate of $OH^\bullet$ radicals was significantly improved. Meanwhile, the desorption of the as-formed H_2O_2 on the Ni_5P_4 surface was also promoted. In addition, the intermediate, $OH^\bullet$ radicals, has been *in-situ* applied for water disinfectant by using tetracycline as an example of contamination. The Ni_5P_4/MB photoanode has presented the best performance for tetracycline degradation, which is in accordance with the performance from H_2O_2 production. The pathway and the resulting compound from the degradation have been studied. It has been found that the resulting compound has presented much lower toxicity than tetracycline. This work develops the TMP materials as co-catalyst to boost photoanodic H_2O_2 production. Also, *in-situ* use of the $OH^\bullet$ radicals for water disinfection has been demonstrated, thus offering opportunities for practical applications.

2. Experimental and method

2.1. Synthesis of Mo doped BiVO₄ photoanodes

The BVO films were synthesized on fluorine-doped tin oxide (FTO) glass substrate *via* the electrochemical deposition method [26]. Firstly, 0.97 g of $Bi(NO_3)_3 \bullet 5H_2O$ was dissolved in a HNO_3 solution (50 mL, pH=1.7). Ultrasonic treatment of the as-prepared solution was carried out for 30 min 3.32 g of KI was then added to the as-prepared solution to achieve a dark-brownish solution. This solution was mixed with the absolute ethanol solution (20 mL) containing 0.5 g of p-benzoquinone. Subsequently, the electrochemical deposition was carried out using a typical three-electrode configuration. In detail, a cleaned FTO glass, a platinum sheet, and a saturated Ag/AgCl electrode were applied as the working electrode, the counter electrode, and the reference electrode, respectively. BiOI films were electrodeposited potentiostatically on FTO glasses at −0.1 V (*vs.* Ag/AgCl) for 3 min. BVO photoanodes were achieved through BiOI films. 150 μL of dimethyl sulfoxide (DMSO) solution containing 0.2 M of vanadyl acetylacetonate ($C_{10}H_{14}O_5V$, 60 μL cm^{-2}) was dropped on as-prepared BiOI films. The films were annealed in a muffle furnace at 450 °C for 2 h to obtain the BVO photoanodes. MB films were also synthesized through drop-coating and calcination. Subsequently, 50 μL of DMSO solution containing 1 % molybdenyl acetylacetonate ($C_{10}H_{16}MoO_6$, molar ratio of Mo to Bi) were dropped on the surface of BVO films. The as-prepared films were calcined in a muffle furnace at 450 °C for 2 h to obtain MB photoanodes.

2.2. Synthesis of metal phosphides particles as co-catalysts

Iron phosphide (Fe_2P), cobalt phosphide (Co_2P), and nickel phosphide (Ni_5P_4) powder were synthesized by a hydrothermal method [27–29]. To synthesize Fe_2P particles, 0.15 g of K_2SO_4 and 0.20 g of $FeCl_3 \cdot H_2O$ were dissolved in 30 mL of H_2O. The as-prepared solution was transferred to a 50 mL Teflon-lined stainless-steel autoclave, which was maintained at 120 °C for 6 h with a heating rate of 5 °C min^{-1}. After cooling to ambient conditions, the as-prepared Fe_2O_3 was dried and

annealed in flowing Ar atmosphere at 450 °C for 3 h to obtain Fe_2O_3 nanoparticles. Fe_2P was synthesized by calcining the Fe_2O_3 (50 mg) powder with $NaH_2PO_2 \cdot H_2O$ (500 mg) powder at 300 °C for 2 h in a tube furnace.

To synthesize Co_2P particles, 1.5 mmol of $Co(NO_3)_2 \cdot 6H_2O$, 7.5 mmol of NH_4F and 5 mmol of $CO(NH_2)_2$ were dissolved in 15 mL of deionized water. The solution was then transferred to a 50 mL Teflon-lined stainless-steel autoclave, which was maintained at 120 °C for 6 h with a heating rate of 5 °C min^{-1} to obtain Co(OH)F. NaH_2PO_2 was blended with Co(OH)F powders in the ratio of 2:1, and annealed at 350 °C in N_2 atmosphere for 4 h to obtain Co_2P.

To synthesize Ni_5P_4 particles, $Ni(OH)_2$ materials were synthesized *via* hydrothermal approach. Specifically, 0.73 g of $Ni(NO_3)_2 \cdot 6 H_2O$, 0.75 g of $CO(NH_2)_2$, and 0.37 g of NH_4F were dissolved in 35 mL of H_2O. The solution was then transferred into a 50 mL Teflon-lined stainless-steel autoclave, which was maintained at 110 °C for 8 h with a heating rate of 5 °C min^{-1}. The as-prepared $Ni(OH)_2$ (50 mg) was mixed with $NaH_2PO_2 \cdot H_2O$ (500 mg), and the as-prepared powder was annealed at 300 °C in flowing Ar atmosphere to obtain the Ni_5P_4 particles.

The as-prepared TMP particles were suspended in water as ink, which was subsequently loaded on the surface of MB photoanodes by drop-coating.

2.3. Characterizations

The photoanodes were studied by X-ray powder diffraction (XRD, MiniFlex 600, Rigaku). The morphology of TMP samples and photoanodes were investigated by a scanning electron microscope (SEM, SU8010, Hitachi). The chemical structure and composition of TMP samples, BVO, MB, and TMP coated MB photoanodes were investigated by a high-resolution transmission electron microscope (HR-TEM) and energy-dispersive X-ray spectroscopy (EDX, FEI Talos). The oxidation states of TMP samples and photoanodes were studied through X-ray photoelectron spectroscopy (XPS, ESCALB 250, Thermofisher Scientific). The binding energies of elements were corrected using C 1 s binding energy (284.8 eV). An ultraviolet-visible-near infrared (UV-Vis-NIR, Cary 500, Varian) spectrophotometer with a small integrating sphere was used to measure the diffuse reflection absorption of the photocatalytic films. Fluorescence lifetime of the photoanodes were measured by time-resolved photoluminescence spectra (TRPL, F-7000 FL, Hitachi). The emission spectra were corrected with the excitation wavelength of 400 nm. The concentration of generated $OH^\bullet$ radicals was measured by an electron paramagnetic resonance spectrometer (EPR, A300 ESR, Bruker) under light illumination. To detect $OH^\bullet$ radicals, 1.0 mg of catalyst powder was suspended in 0.5 mL of 1.0 M $KHCO_3$ solution, and 5 μL of 5,5-dimethyl-1-pyrroline N-oxide (DMPO) was added to the solution to interact with $OH^\bullet$ radicals.

2.4. Photoelectrochemical production of H₂O₂

H_2O_2 was produced using a photoelectrochemical (PEC) system containing an electrochemical workstation (VSP-300, Bio-Logic), a light source of calibrated solar simulator with an AM 1.5 G filter (Sol3A, 94043 A, Newport, USA), and a two-chamber cell with three-electrode system. The as-prepared BVO based photoanode (irradiation area: 1.0 cm^2), a Pt sheet and an Ag/AgCl electrode were used as the working electrode, the counter electrode, and the reference electrode, respectively. The cathodic electrolyte was 0.2 M Na_2SO_4 and the anodic electrolyte was 1.0 M $KHCO_3$ solution (pH = 7.8) [30]. The photoanodic H_2O_2 production reaction was performed using chronoamperometry (CA) with a constant bias of 1.7 V *vs.* RHE under AM 1.5 G illumination. The long-term stability was measured by CA with 1.7 V *vs.* RHE under AM 1.5 G illumination. Linear sweep voltammetry (LSV) was carried out with the bias from 0 V to 2.0 V *vs.* RHE with a scanning rate of 50 mV s^{-1}. The flat band potentials of materials were acquired through Mott-Schottky plots of electrochemical impedance spectroscopy (EIS)

with a range of 1.8–0 V *vs.* RHE [31]. Nyquist plots were acquired through the EIS measurements with the modulation in the frequency range of 200 kHz to 100 mHz under the illumination on or off at 1.7 V *vs.* RHE. The carrier density is calculated using Mott-Schottky relation as Eq. 3 [32]:

$$\frac{1}{C_{SC}^2} = \frac{2}{\varepsilon\varepsilon_0 A^2 e N_d}\left(V - V_{fb} - \frac{K_b T}{e}\right) \tag{3}$$

where C_{sc}^2 is capacitance of space charge region, e is the elementary charge of an electron (1.602×10^{-19} C), ε_0 is the permittivity of vacuum ($\varepsilon_0 = 8.854 \times 10^{-12}$ F m^{-1}), ε is the dielectric constant of BVO ($\varepsilon = 52$) [33], A is the electrochemically active surface area, V is the applied voltage, V_{fb} is flat band potential, and N_d is the donor density.

Incident photon-to-electron conversion efficiency (IPCE) for H_2O_2 production was measured by a 300 W Xenon lamp with a monochromator (QEPVSI-B, Newport, USA) with a scan rate of 360–600 nm. IPCE values were calculated by the Eq. 4 [34]:

$$IPCE(\lambda) = (1240 \bullet j_p(\lambda)) / (\lambda \bullet E_\lambda(\lambda)) \bullet \eta \tag{4}$$

where λ and $E_\lambda(\lambda)$ are the wavelength (nm) and the incident light energy density at a certain wavelength (mW cm^{-2}), respectively. $j_p(\lambda)$ is the steady-state photocurrent density (mA cm^{-2}) at a certain wavelength. η is the selectivity for H_2O_2 production.

The amount of generated H_2O_2 was determined by the Fe^{2+} colorimetric method based on Eq. 5 [35]:

$$Fe^{2+} + H_2O_2 \rightarrow Fe^{3+} + 2OH^- \tag{5}$$

Specifically, 0.9 mL of HCl solution (3.0 M) was added into 1.0 mL of electrolyte containing generated H_2O_2. Subsequently, 0.2 mL of FeSO$_4\cdot$7H$_2$O (0.1 M) was added to the solution. The concentration of obtained H_2O_2 can be determined by the UV–Vis spectrophotometer. The selectivity (η) for H_2O_2 production was calculated using Eq. 6 [36]:

$$\eta \ (\%) = 2 \times N_{H2O2} \times 96485 \ / \ Q \times 100 \tag{6}$$

where N_{H2O2} and Q refer to the amount of produced H_2O_2 and the total amount of charges involved in the reaction, respectively.

The degradation of tetracycline was performed under the same conditions for the H_2O_2 production, and in addition, 50 mg L^{-1} of tetracycline was added to the anodic cell for testing. The electrolyte solutions were bubbled by N_2 for 30 min to remove the O_2. The degradation of tetracycline was probed by UV-Vis NIR spectrophotometer using the wavelength of 370 nm. In addition, the active species, namely OH$^\bullet$, h$^+$, and $^\bullet$O$_2^-$ radicals, for the degradation were investigated using isopropyl alcohol (IPA), ammonium oxalate (AO) and benzoquinone (BQ) solutions with the concentration of 500 mg L^{-1}, respectively. The production after the photoanodic degradation were investigated by the liquid chromatograph mass spectrometer (LC-MS, 1290II-6460, AB5600, Agilent).

3. Results and discussion

3.1. Physicochemical properties of TMPs

The Fe$_2$P, Co$_2$P, and Ni$_5$P$_4$ powder were synthesized by a hydrothermal method, and their crystal structures were probed by XRD as shown in Fig. 1a. Specifically, the Fe$_2$P crystal (JCPDS No. 00–001–1200) presents the peaks centering at 40.4°, 44.6°, 53.2°, and 54.6°, corresponding to the crystal planes of (111), (201), (002), and (211), respectively. The Co$_2$P crystal (JCPDS No. 01–070–8359) shows the peaks centering at 40.7°, 42.0°, and 52.0°, corresponding to the crystal planes of (121), (220), and (230), respectively. The Ni$_5$P$_4$ crystal (JCPDS No. 00–018–0883) shows the peaks centering at 40.6°, 45.1°, 47.8°, and 52.9°, corresponding to the crystal planes of (210), (204), (213), and (214), respectively. The results reveal that by this hydrothermal method, the TMPs can be readily synthesized without any impurities. In addition, the morphology and structure of the TMP powders are studied by SEM as shown in Fig. S1. The sizes of the TMP particles
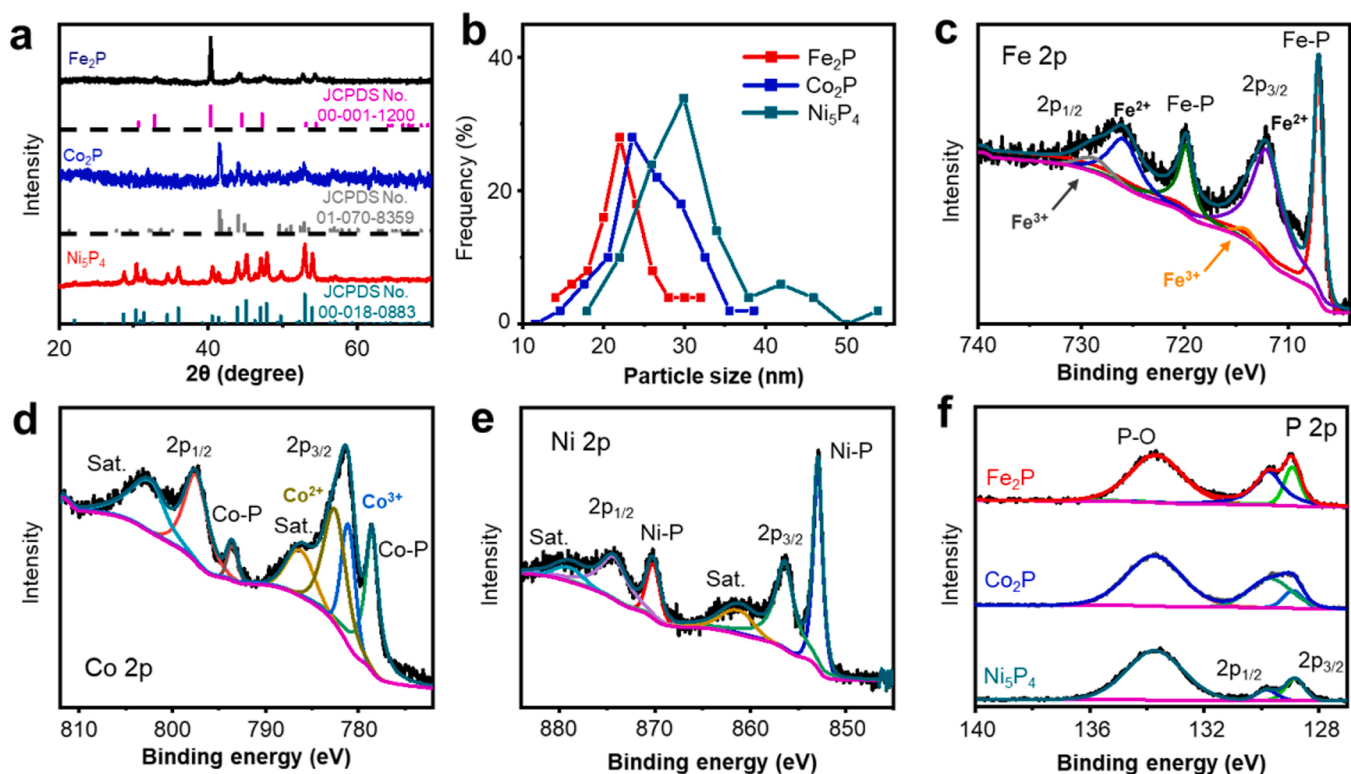

Fig. 1. (a) XRD spectra of Fe$_2$P, Co$_2$P and Ni$_5$P$_4$ crystals. (b) Particle size distribution of Fe$_2$P, Co$_2$P, and Ni$_5$P$_4$ particles. The high-resolution XPS spectra of (c) Fe 2p, (d) Co 2p, and (e) Ni 2p. (f) The high-resolution XPS spectra of P 2p from Fe$_2$P, Co$_2$P and Ni$_5$P$_4$ powders.

are similar and also uniformly distribution. The average particle size is analysed as shown in Fig. 1**b**, and the value ranges between 20 and 30 nm.

XPS was applied to study the chemical properties of the TMP samples. High resolution XPS spectra of Fe 2p, Co 2p, and Ni 2p were shown in Fig. 1**c**–**e**, respectively. In the Fe_2P spectrum, the peaks at 707.1 and 720.0 eV were assigned to the binding energies of Fe $2p_{3/2}$ and Fe $2p_{1/2}$ for iron phosphide, respectively [37]. The other two peaks at 714.1 and 728.7 eV were owing to the iron oxide species. In the Co_2P spectrum, the peaks at 778.4 and 793.5 eV were assigned to the binding energies of Co $2p_{3/2}$ and Co $2p_{1/2}$ for cobalt phosphide, respectively [38], and the peaks at 781.1 eV and 782.7 eV were owing to the cobalt oxide species. In the Ni_5P_4 spectrum, the peaks at 852.9 and 870.3 eV are assigned to the binding energies of Ni $2p_{3/2}$ and Ni $2p_{1/2}$ for nickel phosphide, respectively [39]. In addition, the peaks located at 856.3 eV, 861.5 eV, 874.4 eV, and 879.2 eV were attributed to the nickel oxide species. The XPS spectra of P from the TMPs were shown in Fig. 1**f**. The peaks at 128.8 and 129.9 eV can be attributed to the binding energies of P $2p_{3/2}$ and P $2p_{1/2}$ in metal phosphide, respectively. The extra peak at 133.8 eV was assigned to the phosphate species. Noted that from all the spectra of the TMP samples, the peaks for oxides species were strong. These observations can be attributed to the intrinsic property of the XPS technique as it only collected photoelectrons within the thickness of 1–10 nm from the surface [40], and oxide species are inevitable when the TMP samples are stored in the air.

3.2. TMP co-catalysts coated MB photoanodes

Nano-porous MB films were synthesized on an FTO glass, and the as-prepared TMP powders were loaded on the films by drop-casting of the ink to achieve Fe_2P/MB, Co_2P/MB and Ni_5P_4/MB photoanodes. The concentrations of the TMP were controlled within 0.75, 1.5, 3.0, and 6.0 μg cm^{-2}. Because the size of the TMP particles was nanoscale, they can be anchored on MB films to form stable photoanodes (Fig. 2**a**). The crystal structures of TMP loaded MB films were studied by XRD and compared with MB and BVO (Fig. S2). Typically, owing to the small amount of the TMP co-catalyst, all the spectra present the same peaks (Fig. S2b to S2d). Specifically, the peaks at 18.9°, 28.8°, and 30.5° can be attributed to the (110), (121), and (040) crystal faces of BVO (JCPDS No. 01-075-2480), respectively, and the other peaks at 27.1°, 38.3°, and 51.9° are assigned to (110), (200), and (211) crystal faces of FTO (Fig. S2a, JCPDS No. 00-046-1088).
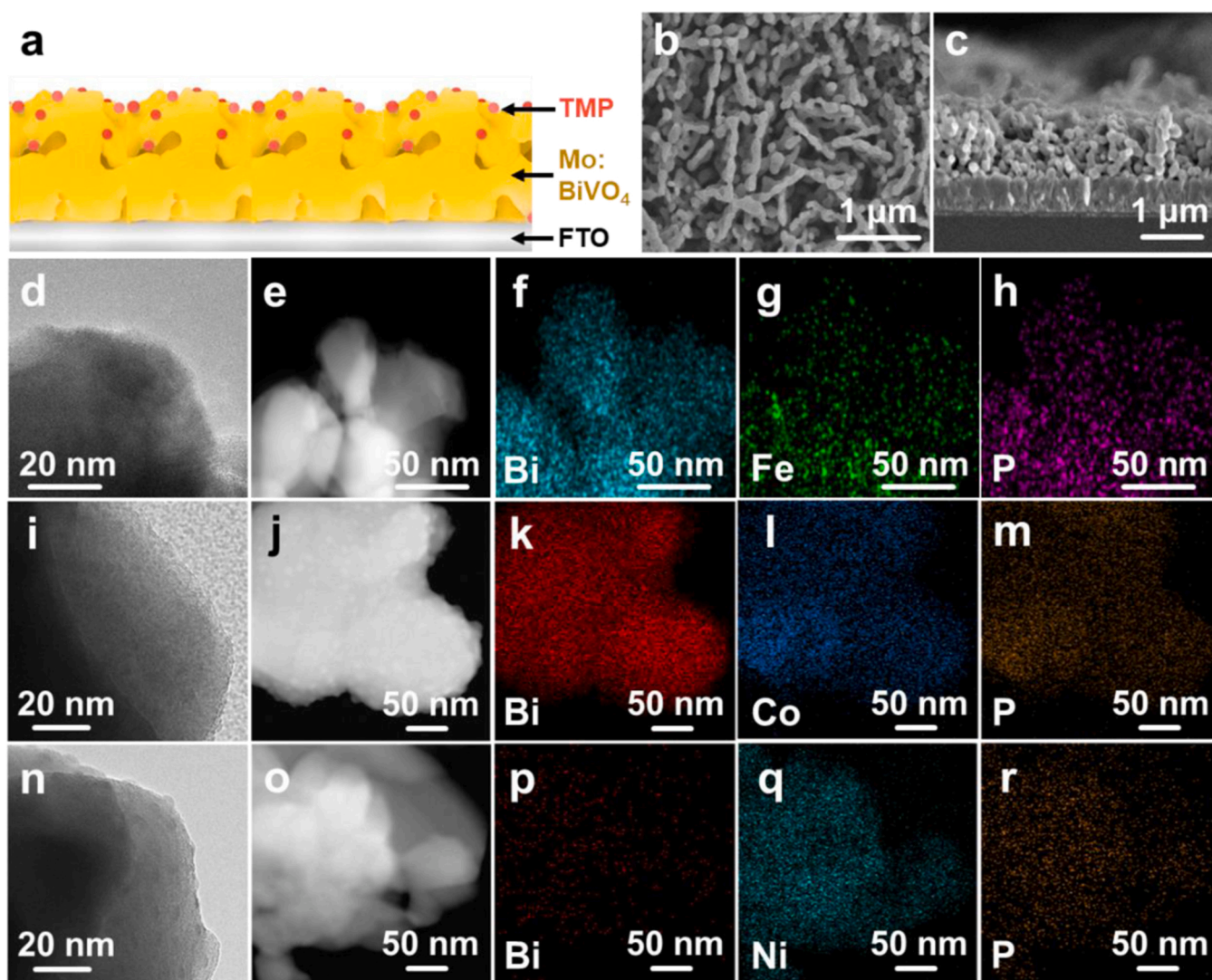

Fig. 2. (a) Schematic illustration of the photoanodic structure, including FTO glass, MB films and TMPs co-catalyst. (b) Top-view and (c) cross-sectional view SEM images of MB films. (d) TEM and (e) HAADF images of Fe_2P/MB materials with the corresponding elemental mappings of (f) Bi, (g) Fe, and (h) P. (i) TEM and (j) HAADF images of Co_2P/MB materials with the corresponding elemental mappings of (k) Bi, (l) Co, and (m) P. (n) TEM and (o) HAADF images of Ni_5P_4/MB materials with the corresponding elemental mappings of (p) Bi, (q) Ni, and (r) P.

Subsequently, SEM and TEM were acquired to study the TMP cocatalyst and the morphology of the photoanodes. The top view and cross-sectional view of the MB films are presented in Fig. 2**b** and **c**, respectively. In comparison, insignificant differences can be realized from TMP loaded photoanodes by SEM (Fig. S3), revealing that the loading of the co-catalyst in such quantity cannot affect the nano-porous structure. The TMP loaded MB films were scratched off for the TEM study, but the TMP co-catalysts are still unobvious as the images shown in Fig. 2**d**, **i**, and **n**, respectively. Therefore, STEM accompanied by EDX was further acquired. Typically, high angle annular dark-field (HAADF) image of the Fe_2P loaded MB films was shown in Fig. 2**e**, and the corresponding elemental mappings of Bi, Fe, P, Mo, V and O are shown in Fig. 2**f** to **h** (Fig. S4a to S4c). In addition, HAADF images of Co_2P and Ni_5P_4 loaded MB films were shown in Fig. 2**j** and **o**, respectively. Correspondingly, the elemental mappings of Bi, Co, P, Mo, V and O are shown in Fig. 2**k** to **m** (Fig. S4d to S4f) for Co_2P loaded MB films, and the elemental mappings of Bi, Ni, P, Mo, V and O are presented in Fig. 2**p** to **r** (Fig. S4g to S4i) for Ni_5P_4 loaded MB films. These observations confirm that the TMP powders, including Fe_2P, Co_2P, and Ni_5P_4, were anchored on the MB films homogeneously.

The light absorption of the photoanodes was studied by UV–vis DRS as the spectra are shown in Fig. S5. It is obvious that either by doping Mo or loading with TMP co-catalyst, the light absorption of the BVO films is insignificantly affected (Fig. S5a, S5c, and S5e), revealing that the small doping quantity of Mo (up to the molar ratio of 1 %) and low loading amount of TMP powder (up to the concentration of ca. 6 µg cm^{-2}) were insufficient to affect the light absorption. Correspondingly, Kubelka-Munk plots were conducted to determine the bandgap (Fig. S5b, S5d, and S5f), and the value is given ca. 2.53 eV, according to the bandgap of BVO materials.

3.3. Photoanodic H_2O_2 production reaction

Photoanodic H_2O_2 production was performed using a typical three-electrode configuration in an electrolyte of 1.0 M $KHCO_3$ solution (pH = 7.8). An AM 1.5 G optical filter was used to stimulate sunlight for illumination. The amount of produced H_2O_2 was determined using a colorimetric method, and the calibration was shown in Fig. S6. LSV curves were collected for H_2O_2 production with the applied bias from 0 to 2.0 V *vs.* RHE as shown in Fig. 3**a**. Noted the fact that doping of Mo increases photocurrent density from 1.3 to 1.6 mA cm^{-2} at 1.7 V (*vs.* RHE). This result is generally known owing to the improved minority charge diffusion length, when V (V) ions were replaced by Mo (VI) ions in the BVO crystal [41]. Moreover, when the TMP co-catalysts were loaded on the MB, the photocurrent density significantly increased, and this fact can be attributed to the promoted surface reaction. The concentration of the loaded co-catalyst has been optimized. The photocurrent density was gradually increased until the loading concentration of the co-catalyst up to ca. 3.0 µg cm^{-2} (Fig. S7), and further increase of the loading co-catalyst becomes ineffective. Correspondingly, the yield and selectivity for H_2O_2 production presented the same trends as photocurrent density (Fig. 3**b** and **c**). As a result, the photoanode with the loading quantity of 3.0 µg cm^{-2} Ni_5P_4 on MB film has presented the optimal photocurrent density, namely ca. 2.7 mA cm^{-2} at 1.7 V (*vs.* RHE). This value is 2.1 times to the pristine BVO photoanode as shown in Fig. 3**a**. The optimal yield and selectivity of Ni_5P_4/MB photoanode for H_2O_2 are 20.8 µmol·h^{-1}·cm^{-2} and 41.9 %, respectively, as shown in Fig. 3**b and c**. In comparison, the pristine BVO only presented the yield and selectivity at ca. 4.6 µmol·h^{-1}·cm^{-2} and 17.9 %, respectively, and MB showed the yield and selectivity at ca. 7.7 µmol·h^{-1}·cm^{-2} and 25.6 %. The optimal yield and selectivity of Fe_2P/MB photoanode were higher than that without any co-catalyst, namely 17.4 µmol·h^{-1}·cm^{-2} and 40.4 %, respectively, and the performance of Co_2P/MB was better than that of Fe_2P/MB photoanode (Fig. 3**b** and S8). The recent reports of the photoanodes for H_2O_2 production are analysed in Table S1, and the performance of this work is comparable to the best of the results.

Subsequently, a two-hour experiment was acquired by the optimal TMP loaded photoanodes as shown in Fig. 3**d**, and all the photoanodes presented similar stability. Specifically, ca. 90 % photocurrent density is reminded, and correspondingly, 90 % yield is preserved for H_2O_2
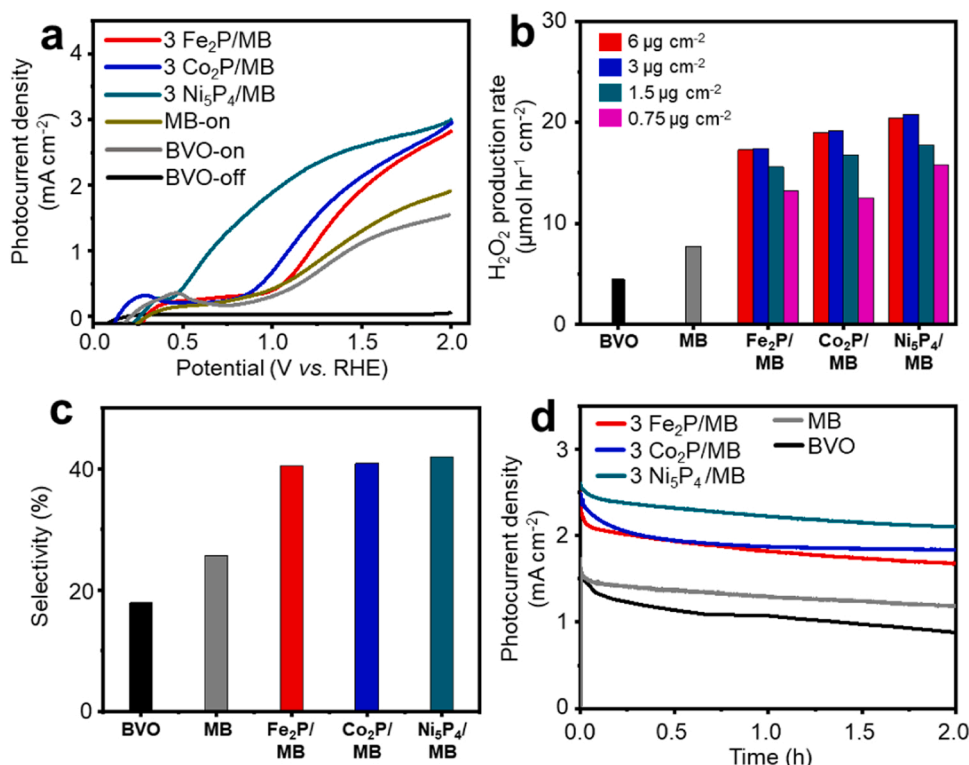

Fig. 3. (a) LSV curves for photoanodic H_2O_2 production. (b) Yield, (c) selectivity, and (d) two-hour CA curve for H_2O_2 production.

production (Fig. S9). The stability of Ni_5P_4 was further confirmed by soaking the Ni_5P_4 powder into a 0.01 M H_2O_2 solution for 24 h, and the as-treated powder was probed by XRD (Fig. S10). The spectra were preserved after the H_2O_2 treatment, indicating that Ni_5P_4 powder was stable in the H_2O_2 solution. The IPCE for the H_2O_2 production and the photocurrent density were acquired at 1.7 V *vs.* RHE with the incident wavelength ranging from 360 to 600 nm (Fig. S11). Generally, the IPCE spectrum is in accordance with the photo-response curve of the BVO based photoanodes (Fig. S5). The highest IPCE value was ca. 22.9 % for H_2O_2 production at the incident wavelength of 360 nm, and correspondingly, the highest IPCE value for the photocurrent density was 56.2 %. In the visible region, the highest IPCE value was ca. 22.6 % at the incident wavelength of 400 nm, and correspondingly, the IPCE value for the photocurrent density was 55.7 %. This result also confirmed that doping Mo into BVO crystal and loading TMP co-catalyst cannot affect the light absorption of the BVO films for photoanodic H_2O_2 production.

3.4. TMP co-catalyst for photoanodic H_2O_2 production

TMP co-catalyst on photoanode is considered to promote the surface reaction for H_2O_2 production, and *in-situ* and steady state experiments were acquired to investigate. Mott-Schottky plots of EIS were performed to study the flat band potentials of the photoanodes (Fig. S12). Since flat band potentials highly associated with the conduction band [42], the conduction bands of all the photoanode can be determined to be ca. 0.1 eV vs RHE (pH = 7.8). With obtaining the bandgap value from UV–vis DRS (Fig. S5), the band structure can be determined from the values of conduction band and valence band, namely 0.1 eV and 2.6 eV, respectively, and this bandgap structure is same as the pristine BVO materials [43]. The results revealed that either doping Mo or loading TMP cocatalysts, the band structure of the photoanode was preserved.

Mo doping in BVO is generally known to improve the charge transfer, and TRPL was applied to study the property of the photoanodes. As the decay curves of the photoluminescence shown in Fig. 4a, with respect to the pristine BVO, the lifetime of the photoexcited charge was significantly reduced from 2.08 ns to 1.95 ns after Mo doping, indicating that the transfer of the photoexcitation charge promoted. When the TMP co-catalysts loaded on the photoanode, minor difference was realized on the lifetimes of the photoexcitation charge, indicating the co-catalyst did not affect the manners of the photoexcitation charge.

Furthermore, Nyquist plots of EIS were performed on the photoanodes during the H_2O_2 production (Figs. S13 and S14), and this *in-situ* characterization was allowed to study both the properties of the photoexcited charge transfer and surface reactions. By fitting the Nyquist spectra with the equivalent circuit, low frequency capacitance (C_{LF}) and low frequency resistance (R_{LF}) can be mainly obtained as the analysis shown in Fig. 4b and S15. Typically, C_{LF} can be understood as the charge accumulation at interface of photoanodes and electrolyte, relating to the kinetics of the surface reaction, which is H_2O_2 production in this case. R_{LF} associates with the photoexcited charge transfer from bulky to the surface of BVO based films. On one hand, minor increase can be realized from C_{LF} when Mo was doped into the BVO crystal, indicating that by the doping, through photocurrent density improves obviously, the surface reaction for H_2O_2 production is minorly promoted. With respect to the Mo doping, the loading of the TMP co-catalyst effectively promotes the surface reaction. Typically, compared with MB ($C_{LF} \sim 1.6 \times 10^{-5}$ F), when Ni_5P_4 loads on the surface, C_{LF} was increased to 8.1×10^{-5} F, which was better than Fe_2P/MB ($C_{LF} \sim 5.9 \times 10^{-5}$ F) and Co_2P/MB ($C_{LF} \sim 6.2 \times 10^{-5}$ F). On the other hand, R_{LF} gradually decreased by doping with Mo and loading TMP co-catalyst. The reduction by Mo doping was known as the improved photoexcited charges transfer, and the reduction by TMP loading indicates that the acceleration of the conversion from H_2O to H_2O_2, and also promotes the charge transfer to the surface, since the photoexcitation charges trends to form equilibrium under light illumination.

The improved surface reaction by TMP co-catalyst is considered as a key to improve the yield and selectivity for photoanodic H_2O_2 production. Therefore, the roles of the TMP in the H_2O_2 production were
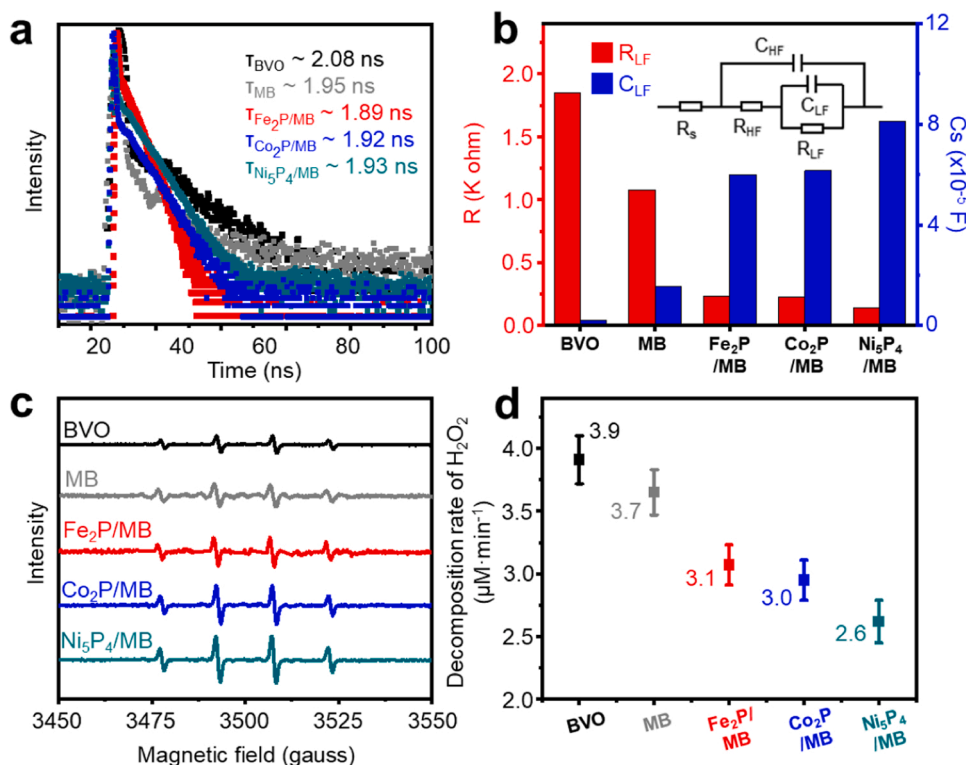

Fig. 4. (a) TRPL spectra of the photoanode. (b) Analyses of the Nyquist plots of EIS by equivalent circuit (inset) for photoanode during the H_2O_2 production (c) EPR spectra of the photoanodes. (d) H_2O_2 desorption from the photoanodes.

investigated. In the conversion of the H_2O to H_2O_2, it is generally known that O-H bonds first dissociated, forming $OH^\bullet$ radical. Subsequently, two of $OH^\bullet$ radicals would couple together to form H_2O_2 molecules. Oxygen evolution reaction as the competition reaction, the O-H bond in $OH^\bullet$ radical can be further dissociated to form $\bullet O^{2-}$, two of which would couple together to form O_2 gas. Therefore, two factors should be mainly considered for the H_2O_2 production. One is the formation rate of the $OH^\bullet$, and the other one is the desorption rate of the formed H_2O_2 from the co-catalyst surface.

EPR were performed to monitor the production rate of $OH^\bullet$. Typically, DMPO was added to interact with the generated $OH^\bullet$ radicals, and the adduct would present quartet peaks with intensity ratio of 1:2:2:1 from EPR. As the spectra shown in Fig. 4c, it is obvious that the intensity of the quartet peaks appears as the order of BVO<MB<Fe_2P/MB<Co_2P/MB<Ni_5P_4/MB photoanodes, revealing that among the co-catalysts, Ni_5P_4 presented highest production rate of $OH^\bullet$ radicals. In addition, this order highly agrees with the yield and selectivity of H_2O_2 production, indicating the production rate of $OH^\bullet$ radicals highly associate with the H_2O_2 production.

In addition, the desorption of H_2O_2 from the co-catalyst was measured [44]. In this study, 5 μL H_2O_2 was added into the to 0.2 M phosphate buffer solution (50 mL), and the photoanodes were inserted into the solution for the testing. The desorption rate can be determined by measuring the reduced concentration of the H_2O_2, since the reduction of H_2O_2 concentration in the electrolyte can be attributed to the adsorption of H_2O_2. If the adsorption rate is slower, the desorption rate is faster. The adsorption of H_2O_2 was measured (Fig. S16), and the

results are analyzed as shown in Fig. 4d. Generally, the desorption rates of BVO and MB were similar, revealing that insignificant difference can be realized for the surface reaction from them. In comparison, by loading TMP cocatalysts, obvious decrease of the decomposition rate was realized, revealing that the co-catalyst improves the desorption of the H_2O_2, which avoids further oxidation for liberation of O_2 gas.

3.5. Photoanodic degradation of tetracycline

H_2O_2 has been widely applied for organic degradation through advanced oxidative processes, and typically, $OH^\bullet$ radicals act as the mediate to drive the organic oxidation reaction. In the photoanodic water oxidation, prior to the formation of the H_2O_2, $OH^\bullet$ radicals forms, and can be applied directly for the oxidation reaction. In this research, tetracycline was investigated as the organic contaminate since it can be widely detected in drinking water [45]. Tetracyclines generally possessed bacteriostatic activity against aerobic and anaerobic bacterial genera. However, it results poor tooth development for the children less than eight years of age easily. The degradation of tetracycline was performed by photoanodic oxidation, as the result shown in Fig. 5a. In this study, tetracycline was added into the anodic electrolyte solution, which was maintained under unilluminated conditions for 30 min till the adsorbing equilibrium [46]. Subsequently, colorimetric method was applied to study the degradation (Fig. S17). The degradation performance is highly accordance with the production rate of the $OH^\bullet$ radicals. For a two-hour experiment, the BVO photoanode retained the 45.7 % of tetracycline, and the optimal Ni_5P_4/MB photoanode retained only 20.8
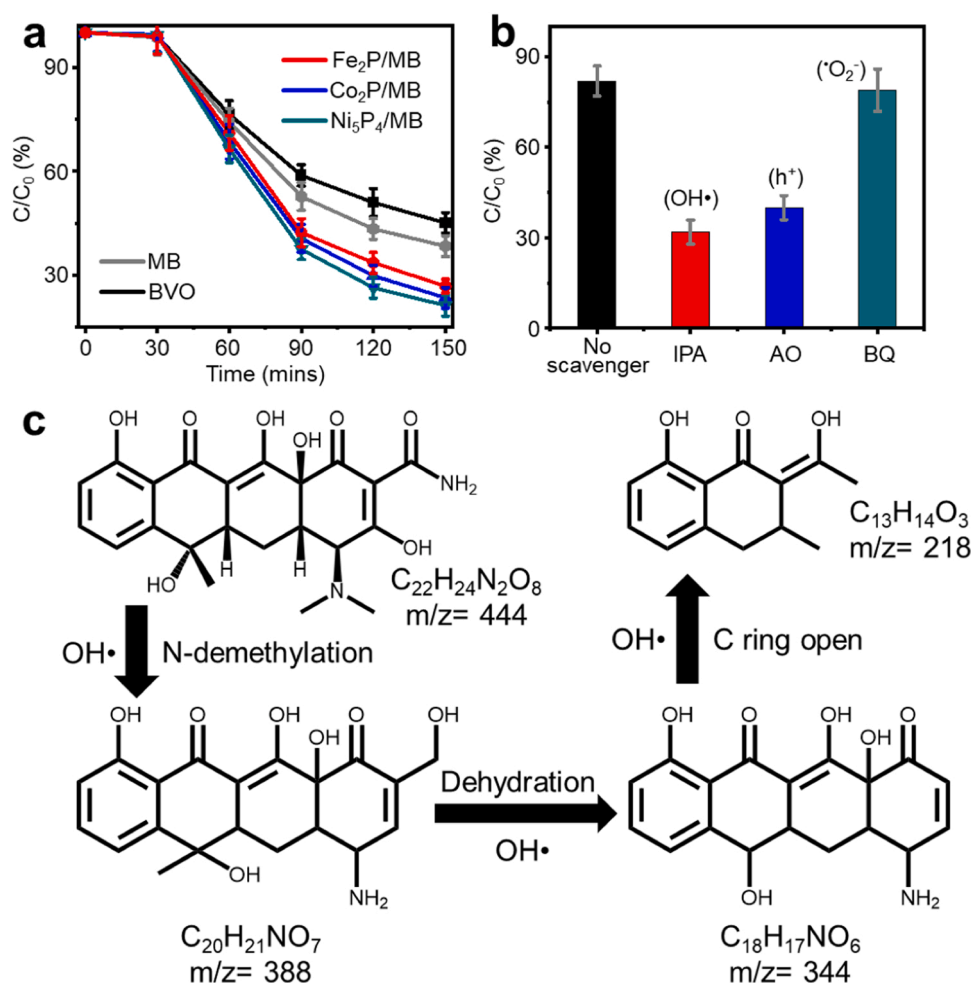

Fig. 5. (a) Adsorption and photoanodic degradation rate of tetracycline. (b) Degradation rate of tetracycline with certain kinds of scavenger by Ni_5P_4/MB photoanode. (c) The possible pathway for tetracycline degradation.

%.

The active species for the degradation were also investigated as shown in Fig. 5**b**. In the electrolyte solution, BQ, AO, and IPA were added as $^\bullet O_2^-$ radical scavenger, hole scavenger, and $OH^\bullet$ radical scavenger, respectively [47]. Obviously, $^\bullet O_2^-$ radical scavenger (BQ) is minor to effect on the degradation performance, indicating the $^\bullet O_2^-$ was not the active species. In a comparison, either adding AO or IPA results significant reduction of the degradation performance. Since the formation of $OH^\bullet$ radical is owing to the dissociation of H-O bond in water molecules by photoexcitation hole, the hole scavenger, AO, would obviously reduce the formation of $OH^\bullet$ radicals and mitigate the degradation rate. In comparison, when $OH^\bullet$ radical scavenger (IPA) was added, the degradation rate become the level similar to that by adding the hole scavenger, indicating the importance of $OH^\bullet$ radical for the degradation.

Moreover, LC-MS was applied to study the resulting compounds after the degradation by Ni_5P_4/MB photoanode (Fig. S18). The molecules with the masses of 445, 388, 344 and 218 Da can be detected, corresponding to the compound (1) tetracycline, (2) $C_{20}H_{21}NO_7$, (3) $C_{18}H_{17}NO_6$, and (4) $C_{13}H_{14}O_3$ likely as shown in Fig. 5**c**. Compound (4) was the main chemical in the resulting solution, and compound (2) and (3) were barely detected [48]. The ratio between compound (4) and tetracycline was ca. 5 from LC-MS test (Fig. S18), and this result agrees with the degradation rate (Fig. 5**a**). As such, the possible pathway for the degradation can be illustrated as shown in Fig. 5**c**. Moreover, the toxicity of the compound (4) was simulated and compared with tetracycline by Toxicity Estimation Software Tool (T.E.S.T., Table S2) [49, 50]. In terms of fathead minnow 50 % lethal concentration (LC_{50}), the concentration of compound (4) is 2.38 mg L^{-1}, which is ca. 6 times to that of tetracycline (0.39 mg L^{-1}). In Ames Mutagenicity test, the tetracycline showed positive with a value of 0.60, and compound (4) shows negative with a value of 0.49. Both stimulations revealed that the toxicity is greatly reduced from this degradation.

4. Conclusions

In a conclusion, three kinds of transition metal phosphide, namely Fe_2P, Co_2P and Ni_5P_4, were applied as co-catalysts to support MB photoanode for H_2O_2 production. The optimal production rate and selectivity were achieved by the Ni_5P_4/MB photoanode, resulting the yield of ca. 20.8 $\mu mol \cdot h^{-1} \cdot cm^{-2}$ and selectivity of ca. 41.9 % at 1.7 V versus reversible hydrogen electrode under sunlight simulator illumination. To the best of the knowledge, this result stood as one of the best performances for photoanodic H_2O_2 production to date, and superior to pristine $BiVO_4$ photoanode. The improved performance can be attributed two key factors, namely, the production rate of $OH^\bullet$ radicals and the promoted desorption of the as-formed H_2O_2. In addition, the intermediates $OH^\bullet$ radicals were *in-situ* applied for tetracycline degradation in water. Compared with other photoanodes, the degradation rate was significantly improved by the Ni_5P_4/MB one. Moreover, the resulting compound from the degradation has been studied, and presented significantly low toxicity than tetracycline. This work has demonstrated the transitional metal phosphide catalyst for the photoanodic water oxidative H_2O_2 production, and the photoanode was applied for *in-situ* water disinfectant.

CRediT authorship contribution statement

Yuntao Xu: Investigation, Methodology, Formal analysis, Data curation, and Writing–original draft. **Yongxin Pan**: Formal analysis, and Data curation. **Yahan Wu**, Investigation, Methodology, and Data curation. **Yuanxing Fang**: Conceptualization, Methodology, Formal analysis, Investigation, Resources, Writing – review & editing, Visualization, Supervision, Project administration, and Funding acquisition. **Masakazu Anpo**: Writing – review & editing. **Hisao Yoshida**: Writing – review & editing. **Xinchen Wang**: Investigation, Supervision, Project administration, and Funding acquisition.

Declaration of Competing Interest

The authors declare that they have no known competing financial interests or personal relationships that could have appeared to influence the work reported in this paper.

Data availability

Data will be made available on request.

Appendix A. Supplementary material

Supplementary data associated with this article can be found in the online version at doi:10.1016/j.apcatb.2023.122701.

References

[1] N. Agarwal, S.J. Freakley, R.U. McVicker, S.M. Althahban, N. Dimitratos, Q. He, D. J. Morgan, R.L. Jenkins, D.J. Willock, S.H. Taylor, C.J. Kiely, G.J. Hutchings, Aqueous Au-Pd colloids catalyze selective CH_4 oxidation to CH_3OH with O_2 under mild conditions, Science 358 (2017) 223–227.

[2] M. Yamada, K.D. Karlin, S. Fukuzumi, One-step selective hydroxylation of benzene to phenol with hydrogen peroxide catalysed by copper complexes incorporated into mesoporous silica–alumina, Chem. Sci. 7 (2016) 2856–2863.

[3] S. Naniwa, A. Yamamoto, H. Yoshida, Visible light-induced Minisci reaction through photoexcitation of surface Ti-peroxo species, Catal. Sci. Technol. 11 (2021) 3376–3384.

[4] E. Ouahiba, M. Chabani, A.A. Assadi, A. Abdeltif, F. Florence, B. Souad, Mineralization and photodegradation of oxytetracycline by $UV/H_2O_2/Fe^{2+}$ and $UV/PS/Fe^{2+}$ process: quantification of radicals, Res. Chem. Inter. (2022), https://doi.org/10.1007/s11164-11022-04871-x.

[5] A. Khorshidi, N. Mardazad, Flower-like silver nanoparticles: an effective and recyclable catalyst for degradation of Rhodamine B with H_2O_2, Res. Chem. Intermed. 42 (2016) 7551–7558.

[6] Y. Lin, A. Hou, H. Li, C. Shi, L. Chen, B. Yuan, Y. Liu, Y. Wang, X. Liu, Synergistic and efficient degradation of acid red 73 by using UV, H_2O_2, and PDS under neutral conditions: water matrix effects and transformation pathways, Res. Chem. Inter. (2022), https://doi.org/10.1007/s11164-11022-04870-y.

[7] L. Li, K. Xiao, P.K. Wong, Z. Hu, J.C. Yu, Hydrogen peroxide production from water oxidation on a $CuWO_4$ anode in oxygen-deficient conditions for water decontamination, ACS Appl. Mater. Interfaces 14 (2022) 7878–7887.

[8] S. Yang, A. Verdaguer-Casadevall, L. Arnarson, L. Silvioli, V. Čolić, R. Frydendal, J. Rossmeisl, I. Chorkendorff, I.E.L. Stephens, Toward the decentralized electrochemical production of H_2O_2: a focus on the catalysis, ACS Catal. 8 (2018) 4064–4081.

[9] W. Jiang, Y. An, Z. Wang, M. Wang, X. Bao, L. Zheng, H. Cheng, P. Wang, Y. Liu, Z. Zheng, Y. Dai, B. Huang, Stress-induced $BiVO_4$ photoanode for enhanced photoelectrochemical performance, Appl. Catal. B 304 (2022), 121012.

[10] K. Iyatani, Y. Horiuchi, M. Moriyasu, S. Fukumoto, S.-H. Cho, M. Takeuchi, M. Matsuoka, M. Anpo, Development of separate-type Pt-free photofuel cells based on visible-light responsive TiO_2 photoanode, J. Mater. Chem. 22 (2012) 10460–10463.

[11] K. Iyatani, Y. Horiuchi, S. Fukumoto, M. Takeuchi, M. Anpo, M. Matsuoka, Separate-type Pt-free photofuel cell based on a visible light-responsive TiO_2 photoanode: effect of hydrofluoric acid treatment of the photoanode, Appl. Catal. A-Gen. 458 (2013) 162–168.

[12] Y. Li, Q. Mei, Z. Liu, X. Hu, Z. Zhou, J. Huang, B. Bai, H. Liu, F. Ding, Q. Wang, Fluorine-doped iron oxyhydroxide cocatalyst: promotion on the WO_3 photoanode conducted photoelectrochemical water splitting, Appl. Catal. B 304 (2022), 120995.

[13] F. Amano, B. Ohtani, H. Yoshida, Role of doped titanium species in the enhanced photoelectrochemical properties of iron oxide films: Comparison between water oxidation and iodide ion oxidation, J. Electroanal. Chem. 766 (2016) 100–106.

[14] L. Wang, Y. Kong, Y. Fang, P. Cai, W. Lin, X. Wang, A Ga doped $NiTiO_3$ photocatalyst for overall water splitting under visible light illumination, Adv. Funct. Mater. 32 (2022), 2208101.

[15] Y. Fang, Y. Xu, X. Li, Y. Ma, X. Wang, Coating polymeric carbon nitride photoanodes on conductive Y:ZnO nanorod arrays for overall water splitting, Angew. Chem. Int. Ed. 57 (2018) 9749–9753.

[16] Z. Chen, Y. Fang, L. Wang, X. Chen, W. Lin, X. Wang, Remarkable oxygen evolution by Co-doped ZnO nanorods and visible light, Appl. Catal. B: Environ. 296 (2021), 120369.

[17] K. Zhang, J. Liu, L. Wang, B. Jin, X. Yang, S. Zhang, J.H. Park, Near-complete suppression of oxygen evolution for photoelectrochemical H_2O oxidative H_2O_2 synthesis, J. Am. Chem. Soc. 142 (2020) 8641–8648.

[18] Y. Miyase, S. Takasugi, S. Iguchi, Y. Miseki, T. Gunji, K. Sasaki, E. Fujita, K. Sayama, Modification of $BiVO_4$/WO_3 composite photoelectrodes with Al_2O_3 via chemical vapor deposition for highly efficient oxidative H_2O_2 production from H_2O, Sustain. Energy Fuels 2 (2018) 1621–1629.

[19] J. Zhang, X. Chang, Z. Luo, T. Wang, J. Gong, A highly efficient photoelectrochemical H_2O_2 production reaction with Co_3O_4 as a co-catalyst, Chem. Commun. 54 (2018) 7026–7029.

[20] L. Yang, H. Chen, Y. Xu, R. Qian, Q. Chen, Y. Fang, Synergetic effects by Co^{2+} and PO_4^{3-} on Mo-doped $BiVO_4$ for an improved photoanodic H_2O_2 evolution, Chem. Eng. Sci. 251 (2022), 117435.

[21] Y. Xu, Y. Cao, L. Tan, Q. Chen, Y. Fang, The development of cobalt phosphide co-catalysts on $BiVO_4$ photoanodes to improve H_2O_2 production, J. Colloid Interface Sci. 633 (2023) 323–332.

[22] M. Jiang, W. Fan, A. Zhu, P. Tan, J. Xie, J. Pan, Ion-biosorption induced core–shell Fe_2P@carbon nanoparticles decorated on N, P co-doped carbon materials for the oxygen evolution reaction, Inorg. Chem. Front. 8 (2021) 2385–2394.

[23] Y. Li, Y. Wu, H. Hao, M. Yuan, Z. Lv, L. Xu, B. Wei, In situ unraveling surface reconstruction of Ni_5P_4@FeP nanosheet array for superior alkaline oxygen evolution reaction, Appl. Catal. B 305 (2022), 121033.

[24] M. Zhu, Y. Zhou, Y. Sun, C. Zhu, L. Hu, J. Gao, H. Huang, Y. Liu, Z. Kang, Cobalt phosphide/carbon dots composite as an efficient electrocatalyst for oxygen evolution reaction, Dalton Trans. 47 (2018) 5459–5464.

[25] J. Yang, F. Zhang, X. Wang, D. He, G. Wu, Q. Yang, X. Hong, Y. Wu, Y. Li, Porous molybdenum phosphide nano-octahedrons derived from confined phosphorization in UIO-66 for efficient hydrogen evolution, Angew. Chem., Int. Ed. 55 (2016) 12854–12858.

[26] T.W. Kim, K.-S. Choi, Nanoporous $BiVO_4$ photoanodes with dual-layer oxygen evolution catalysts for solar water splitting, Science 343 (2014) 990–994.

[27] L. Liao, C. Cheng, H. Zhou, Y. Qi, D. Li, F. Cai, B. Yu, R. Long, F. Yu, Accelerating pH-universal hydrogen-evolving activity of a hierarchical hybrid of cobalt and dinickel phosphides by interfacial chemical bonds, Mater. Today Phys. 22 (2022), 100589.

[28] X. Shi, P. An, Q. Zhang, Q. Song, D. Jiang, D. Tian, D. Li, Synergy of nitrogen vacancies and Fe_2P cocatalyst on graphitic carbon nitride for boosting photocatalytic CO_2 conversion, Chem. Eng. J. 446 (2022), 137096.

[29] X. Liu, Y. Zhao, X. Yang, Q. Liu, X. Yu, Y. Li, H. Tang, T. Zhang, Porous Ni_5P_4 as a promising cocatalyst for boosting the photocatalytic hydrogen evolution reaction performance, Appl. Catal. B 275 (2020), 119144.

[30] X. Shi, Y. Zhang, S. Siahrostami, X. Zheng, Light-driven $BiVO_4$–C fuel cell with simultaneous production of H_2O_2, Adv. Energy Mater. 8 (2018), 1801158.

[31] L. Wang, P. Cai, Z. Liu, Z. Xie, Y. Fang, Role of carbon quantum dots on Nickel titanate to promote water oxidation reaction under visible light illumination, J. Colloid Interf. Sci. 607 (2022) 203–209.

[32] X. Li, J. Wang, J. Xia, Y. Fang, Y. Hou, X. Fu, M. Shalom, X. Wang, One-pot synthesis of CoS_2 merged in polymeric carbon nitride films for photoelectrochemical water splitting, Chemsuschem 15 (2022), e202200330.

[33] T.W. Kim, Y. Ping, G.A. Galli, K.-S. Choi, Simultaneous enhancements in photon absorption and charge transport of bismuth vanadate photoanodes for solar water splitting, Nat. Commun. 6 (2015) 8769.

[34] X. Li, X. Chen, Y. Fang, W. Lin, Y. Hou, M. Anpo, X. Fu, X. Wang, High-performance potassium poly(heptazine imide) films for photoelectrochemical water splitting, Chem. Sci. 13 (2022) 7541–7551.

[35] K. Fuku, K. Sayama, Efficient oxidative hydrogen peroxide production and accumulation in photoelectrochemical water splitting using a tungsten trioxide/ bismuth vanadate photoanode, Chem. Commun. 52 (2016) 5406–5409.

[36] C. Ampelli, F. Tavella, C. Genovese, S. Perathoner, M. Favaro, G. Centi, Analysis of the factors controlling performances of Au-modified TiO_2 nanotube array based photoanode in photo-electrocatalytic (PECa) cells, J. Energy Chem. 26 (2017) 284–294.

[37] Y. Yao, N. Mahmood, L. Pan, G. Shen, R. Zhang, R. Gao, F.-E. Aleem, X. Yuan, X. Zhang, J.-J. Zou, Iron phosphide encapsulated in P-doped graphitic carbon as efficient and stable electrocatalyst for hydrogen and oxygen evolution reactions, Nanoscale 10 (2018) 21327–21334.

[38] Y. Yan, J. Huang, X. Wang, T. Gao, Y. Zhang, T. Yao, B. Song, Ruthenium incorporated cobalt phosphide nanocubes derived from a prussian blue analog for enhanced hydrogen evolution, Front. Chem. 6 (2018) 521.

[39] X. Xiao, X. Wu, Y. Wang, K. Zhu, B. Liu, X. Cai, T. Yang, X. Xu, D. Zhang, Co-doped porous Ni_5P_4 nanoflower: an efficient hydrogen evolution electrocatalyst with high activity and electrochemical stability, Catal. Commun. 138 (2020) 105957.

[40] D.R. Baer, Y.-C. Wang, D.G. Castner, Use of XPS to quantify thickness of coatings on nanoparticles, Microsc. Today 24 (2016) 40–45.

[41] J.A. Seabold, K. Zhu, N.R. Neale, Efficient solar photoelectrolysis by nanoporous Mo:$BiVO_4$ through controlled electron transport, Phys. Chem. Chem. Phys. 16 (2014) 1121–1131.

[42] A. Hankin, F.E. Bedoya-Lora, J.C. Alexander, A. Regoutz, G.H. Kelsall, Flat band potential determination: avoiding the pitfalls, J. Mater. Chem. A 7 (2019) 26162–26176.

[43] W. Fang, Y. Lin, R. Xv, X. Shang, L. Fu, Band-gap and interface engineering by Ni doping and CoPi deposition of $BiVO_4$ photoanode to boost photoelectrochemical water splitting, Electrochim. Acta 437 (2023), 141511.

[44] T.H. Jeon, H. Kim, H.-I. Kim, W. Choi, Highly durable photoelectrochemical H_2O_2 production via dual photoanode and cathode processes under solar simulating and external bias-free conditions, Energ. Environ. Sci. 13 (2020) 1730–1742.

[45] Z. Li, C. Guo, J. Lyu, Z. Hu, M. Ge, Tetracycline degradation by persulfate activated with magnetic Cu/$CuFe_2O_4$ composite: Efficiency, stability, mechanism and degradation pathway, J. Hazard. Mater. 373 (2019) 85–96.

[46] A.V. Karim, S. Krishnan, A. Shriwastav, Sonocatalytic degradation of tetracycline with Cu-doped TiO_2 nanoparticles as the catalyst: optimization, kinetics, and mechanism, Water Air Soil Pollut. 234 (2023) 41.

[47] Y. Zou, M. Zhang, P. Huang, P. Zhao, X. Yang, S. Xie, H. Chen, M. Zhang, F. Cheng, Enhanced photoelectrochemical degradation of toxic tetracycline by Au nanoparticles modified Co doped Fe_2O_3 electrode under mild conditions, Mater. Lett. 327 (2022), 133004.

[48] M. Nie, Y. Li, J. He, C. Xie, Z. Wu, B. Sun, K. Zhang, L. Kong, J. Liu, Degradation of tetracycline in water using Fe_3O_4 nanospheres as Fenton-like catalysts: kinetics, mechanisms and pathways, N. J. Chem. 44 (2020) 2847–2857.

[49] H. Zeng, S. Shen, A. Cai, Q. Sun, L. Wang, S. Zhu, X. Li, J. Deng, Degradation of tetracycline by UV/Fe^{3+}/persulfate process: Kinetics, mechanism, DBPs yield, toxicity evaluation and bacterial community analysis, Chemosphere 307 (2022), 136072.

[50] X. Ao, W. Sun, S. Li, C. Yang, C. Li, Z. Lu, Degradation of tetracycline by medium pressure UV-activated peroxymonosulfate process: Influencing factors, degradation pathways, and toxicity evaluation, Chem. Eng. J. 361 (2019) 1053–1062.